Continuous Mott transition in semiconductor moiré superlattices

https://doi.org/10.1038/s41586-021-03853-0

Received: 3 March 2021

Accepted: 22 July 2021

Published online: 15 September 2021

Check for updates

Tingxin Li[1,6], Shengwei Jiang[2,6], Lizhong Li[1,6], Yang Zhang[3], Kaifei Kang[1], Jiacheng Zhu[1], Kenji Watanabe[4], Takashi Taniguchi[4], Debanjan Chowdhury[2], Liang Fu[3], Jie Shan[1,2,5]✉ & Kin Fai Mak[1,2,5]✉

The evolution of a Landau Fermi liquid into a non-magnetic Mott insulator with increasing electronic interactions is one of the most puzzling quantum phase transitions in physics[1–6]. The vicinity of the transition is believed to host exotic states of matter such as quantum spin liquids[4–7], exciton condensates[8] and unconventional superconductivity[1]. Semiconductor moiré materials realize a highly controllable Hubbard model simulator on a triangular lattice[9–22], providing a unique opportunity to drive a metal–insulator transition (MIT) via continuous tuning of the electronic interactions. Here, by electrically tuning the effective interaction strength in $MoTe_2/WSe_2$ moiré superlattices, we observe a continuous MIT at a fixed filling of one electron per unit cell. The existence of quantum criticality is supported by the scaling collapse of the resistance, a continuously vanishing charge gap as the critical point is approached from the insulating side, and a diverging quasiparticle effective mass from the metallic side. We also observe a smooth evolution of the magnetic susceptibility across the MIT and no evidence of long-range magnetic order down to ~5% of the Curie–Weiss temperature. This signals an abundance of low-energy spinful excitations on the insulating side that is further corroborated by the Pomeranchuk effect observed on the metallic side. Our results are consistent with the universal critical theory of a continuous Mott transition in two dimensions[4,23].

The interaction induced localization of electrons—the Mott transition—is expected to occur in the half-filled Hubbard model[1–3,24,25]. The ground state is a metal with a sharply defined electronic Fermi surface when the kinetic energy of the electrons—characterized by the bandwidth W—far exceeds their interaction energy—characterized by the on-site Coulomb repulsion U. Conversely, when $U \gg W$, the ground state is an electrical insulator with a charge gap. The system undergoes a MIT when U and W become comparable. Although this picture is widely accepted from the seminal works of Mott and Hubbard, the nature of the transition remains poorly understood. In most materials, the transitions are driven first-order and often accompanied by simultaneous magnetic, structural or other forms of ordering[1,3]. Continuous MIT, which exhibits no symmetry breaking, an abrupt disappearance of an entire electronic Fermi surface and the simultaneous opening of a charge gap across a quantum critical point, remains one of the outstanding problems in condensed matter physics[1–6,26–28]. Despite the extensive theoretical studies on the topic[1–8,23–29], experimental candidates remain scarce[1].

Continuous Mott transitions are generally favoured by geometric frustration and reduced dimensionality, where strong quantum fluctuations can weaken or even quench different types of order[3,4,28–31]. Moiré heterostructures of two-dimensional (2D) semiconducting transition metal dichalcogenides (TMDs), which are believed to realize a triangular lattice Hubbard model[9,19,20], provide an ideal testbed of the Mott transition[21,22]. The system is highly controllable—allowing independent tuning of both the filling factor and the effective interaction strength (U/W). In particular, the electron density can be continuously tuned by gating in field-effect devices[10–16]. The effective interaction strength can be tuned, in principle, by varying the twist angle between the TMD layers[9,20], which determines the moiré period and thus the bandwidth. Here we demonstrate continuous tuning of U/W by an out-of-plane electric field. The electric field varies the potential difference between the two TMD layers and subsequently the moiré potential, which changes the size of the localized Wannier function and the bandwidth predominantly (Methods). We investigate the electrical transport and magnetic properties of the system at fixed half-band filling as a function of effective interaction.

Electric-field-tuned MITs

We investigate near-zero-degree-aligned $MoTe_2/WSe_2$ heterobilayers with hole doping. The two TMD materials have ~7% lattice mismatch. At zero twist angle they form a triangular moiré superlattice with period of ~5 nm (Fig. 1a), which corresponds to a moiré density of ~5×10^{12} cm^{-2}. In each TMD monolayer, the band edges are located at the K/K′ points of the Brillouin zone with double spin-valley degeneracy. The electronic band structures of relaxed zero-degree-aligned $MoTe_2/WSe_2$

[1]School of Applied and Engineering Physics, Cornell University, Ithaca, NY, USA. [2]Laboratory of Atomic and Solid State Physics, Cornell University, Ithaca, NY, USA. [3]Department of Physics, Massachusetts Institute of Technology, Cambridge, MA, USA. [4]National Institute for Materials Science, Tsukuba, Japan. [5]Kavli Institute at Cornell for Nanoscale Science, Ithaca, NY, USA. [6]These authors contributed equally: Tingxin Li, Shengwei Jiang and Lizhong Li. ✉e-mail: jie.shan@cornell.edu; kinfai.mak@cornell.edu

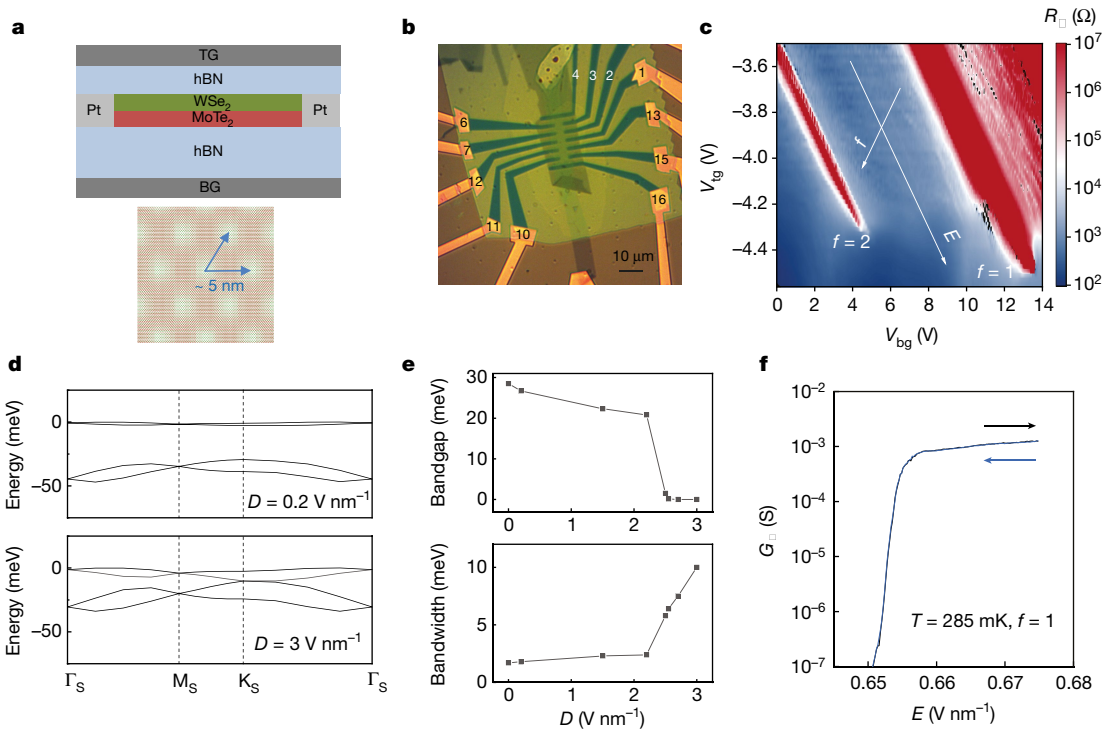

Fig. 1 | Bandwidth-tuned metal-insulator transition. a, Top: schematic side view of $MoTe_2/WSe_2$ moiré heterobilayer devices with hBN/graphite gates and Pt contact electrodes. Bottom: the moiré superlattice with 5 nm moiré period. **b**, Optical microscope image of multi-terminal Hall bar device 1. The scale bar represents 10 μm. **c**, Square resistance of device 1 at 300 mK in logarithmic scale as a function of top and bottom gate voltages. The gate voltages relate to the hole filling factor f and electric field E (field direction is up in **a**). Electric-field-induced MIT is observed at $f = 1$ and 2. **d**, Electronic band structure (first two hole moiré bands) of zero-degree-aligned $MoTe_2/WSe_2$ heterobilayers from DFT under displacement field $D = 0.2$ V nm^{-1} (top) and 3.0 V nm^{-1} (bottom). **e**, Bandgap between the first and second moiré bands (top) and bandwidth of the first moiré bands (bottom) as a function of displacement field from DFT. **f**, Square conductance at $f = 1$ as a function of electric field near the MIT at 285 mK. No hysteresis is observed under forward and backward scans of the electric field.

heterobilayers are characterized by density functional theory (DFT) (Methods). They have type-I band alignment with valence band offset of ~300 meV (both conduction and valence band edges are from $MoTe_2$). Figure 1d illustrates the first two moiré valence bands under two values of out-of-plane displacement field, D, that reduces the valence band offset. The displacement field strongly affects the band dispersions. The bandwidth of the first moiré band increases rapidly with D for sufficiently large fields (Fig. 1e), supporting the feasibility of bandwidth-tuned MITs. The large lattice mismatch of the two materials has several practical advantages. The heterostructures are less prone to effects of disorders from angle alignment inhomogeneities since the moiré period is not sensitive to twist angle near zero degree. The large moiré density or, equivalently, doping density, at half filling compared to the disorder density (~10^{11} cm^{-2}; Methods) favours purely interaction-driven MITs. Finally, the large doping density facilitates the formation of good electrical contacts for transport measurements at low temperatures.

We fabricate dual-gate field-effect devices of $MoTe_2/WSe_2$ heterobilayers with hexagonal boron nitride (hBN) gate dielectrics and graphite gate electrodes (Fig. 1a, b). The typical hBN thickness is about 5 nm and 20–30 nm, respectively, in the top and bottom gates. We pattern the devices into Hall bar geometry and measure the four-point sheet resistance down to 300 mK (see Methods for device fabrication and measurements). Figure 1c shows square resistance $R_\square$ of device 1 at 300 mK as a function of two gate voltages. It can be converted to resistance as a function of filling factor f and applied out-of-plane electric field E (average of the top and bottom electric fields) using the known device geometry (Extended Data Fig. 1). The two prominent resistance features correspond to $f = 1$ and 2, respectively, where $f = 1$ denotes one hole per moiré cell, that is, half filling of the first moiré valence band. The insulating states at $f = 1$ and 2 are the known Mott and band insulating states, respectively[10–16]. At sufficiently large applied fields they both turn metallic. The MIT at $f = 2$ occurs at a smaller field (Extended Data Fig. 2). Its mechanism is distinct from that of the Mott transition at $f = 1$. The applied field closes the gap between the first and second moiré bands and induces a transition from a band insulator to a compensated semi-metal. It induces no observable effects on the Mott insulating state (see Methods on effects of remote moiré bands).

The continuous Mott transition

Below we focus on the interaction (or bandwidth) driven MIT at $f = 1$. The sheet resistance or conductance ($G_\square = 1/R_\square$) is sensitive to applied electric field near the transition; at the lowest temperature (285 mK), it changes by more than four orders of magnitude within a narrow range of the critical field $E_c \approx 0.652$ V nm^{-1} (Fig. 1f). No hysteresis is observed for different sweeping directions of the field.

Figure 2a illustrates the temperature dependences of resistance up to 70 K at representative electric fields. They show two types of behaviours. Below the critical field, the resistance increases upon cooling. This is characteristic of an insulator. The resistance follows a thermal activation dependence (Extended Data Fig. 3). We extract the activation gap Δ for charge transport in Fig. 2b. The gap size decreases monotonically from tens of meV to a few meV as E_c is approached from below. It follows a power-law dependence $\Delta \propto |E - E_c|^{\nu z}$ with exponent $\nu z \approx 0.60 \pm 0.05$ (Fig. 2c).

Above the critical electric field, the resistance follows a T^2 dependence at low temperatures over a range up to ~10 K. This is characteristic of a

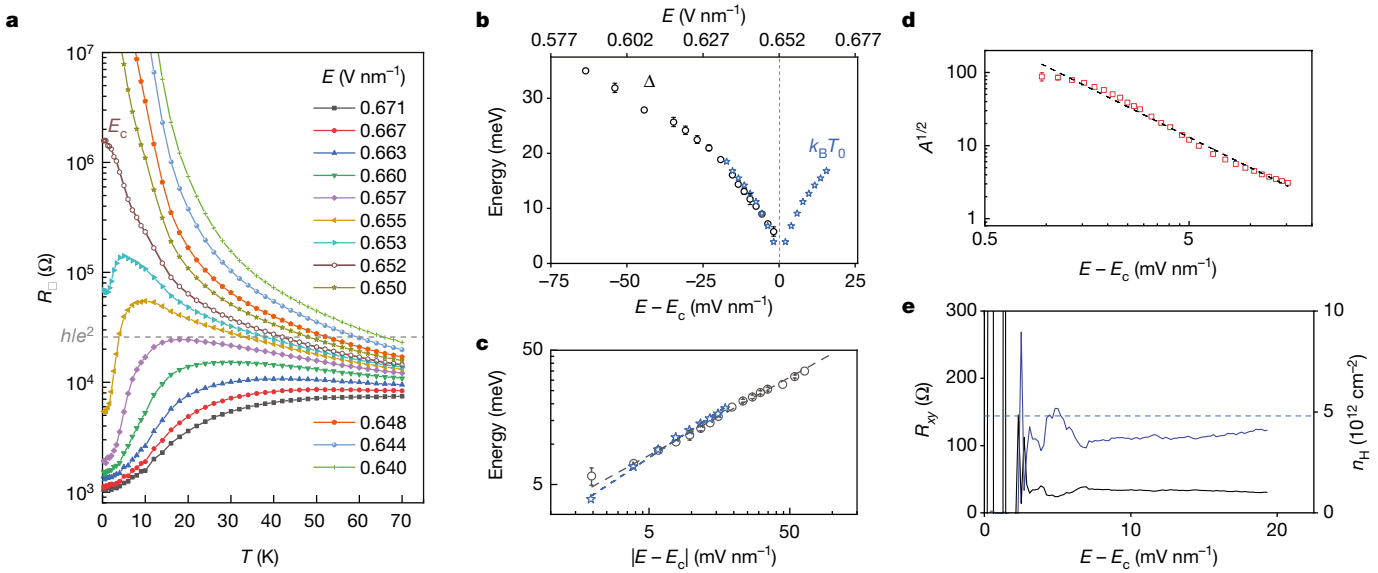

Fig. 2 | Continuous Mott transition. a, Temperature dependence of square resistance (symbols) at fixed filling factor $f = 1$ under varying electric fields. The lines are a guide to the eye. The resistance at the critical electric field $E_c = 0.652$ V nm^{-1} (open symbols) follows a power-law dependence. The horizontal dashed line marks the resistance quantum. **b**, **c**, Continuously vanishing charge gap Δ and temperature scaling parameter T_0 (multiplied by the Boltzmann constant k_B) as the electric field E approaches the critical field E_c. Both follow a power-law dependence on $|E - E_c|$ with nearly identical exponents (**c**). **d**, Electric-field dependence of $A^{1/2}$ in a log–log plot, where A is the fitting parameter for the low-temperature square resistance ($R_\square = R_0 + AT^2$ with R_0 denoting the residual resistance) and the error bars are the fitting uncertainty. The dashed line is a power-law fit $A^{1/2} \propto |E - E_c|^{-1.4\pm0.1}$. **e**, Electric-field dependence of the Hall resistance R_{xy} and Hall density n_H above E_c. The Hall density is largely field independent and consistent with the moiré density (horizontal dashed line). It is obtained from Hall measurements under ±0.2 T, followed by anti-symmetrizing the response. The magnetic-field-induced MIT (Fig. 4c) prevents reliable measurements close to E_c.

Landau Fermi liquid with electron–electron umklapp scattering. We fit the low-temperature resistance with $R_\square = R_0 + AT^2$ (Extended Data Fig. 3), where R_0 denotes the residual resistance and $A^{1/2}$ is proportional to the quasiparticle effective mass m^* according to Kadowaki–Woods scaling[32]. The electric-field dependence of $A^{1/2}$ is well described by a power-law divergence, $A^{1/2} \propto m^* \propto |E - E_c|^{-1.4\pm0.1}$, as E approaches E_c from above (Fig. 2d). The mass divergence is contrasted by the weak electric-field dependence of the Hall density (Fig. 2e). The result suggests that the entire electronic Fermi surface contributes to transport, with m^* diverging at E_c due to quantum fluctuations near the MIT[2–4,23,24,29].

The resistance deviates from the T^2 dependence at higher temperatures; it reaches a maximum at temperature T^* and decreases with further increase of temperature. The insulating-like behaviour here follows a power law rather than an activation temperature dependence (Extended Data Fig. 4). The value of T^* decreases upon approaching the MIT (Fig. 3c). The square resistance can exceed the Mott–Ioffe–Regel limit (horizontal dashed line in Fig. 2a), h/e^2, with h and e denoting, respectively, the Planck's constant and the elementary charge. This corresponds to a mean free path smaller than the moiré period and is suggestive of 'bad' metallic behaviour[33].

Next we demonstrate quantum critical scaling collapse of the resistance curves near the MIT. We first identify the precise value of the critical field at which a simple power-law dependence of $R_\square(T)$ is observed (Extended Data Fig. 4). We normalize $R_\square(T)$ by resistance at the critical field $R_c(T)$. The resistance curves near the MIT collapse onto two branches after the temperatures are scaled by field-dependent T_0s (Fig. 3a, b, see Supplementary Information for details). The top and bottom branches represent the insulating and metallic transport behaviours, respectively; they display reflection symmetry about $R_\square/R_c = 1$ in the log–log plot. We fix the scale of T_0 by matching it to the measured charge gap at one field on the insulating side. The same T_0s are used to scale the curves on the metallic side of equal distance to the critical point without any adjustment. The scaling parameter T_0 continuously vanishes as it approaches the critical field (Fig. 2b). Similar to the charge gap, T_0 follows a power-law dependence $T_0 \propto |E - E_c|^{\nu z}$ with exponent $\nu z \approx 0.70 \pm 0.05$ (Fig. 2c). Figure 3a, b also compares two sets of measurements of the same device after different thermal cycles; the behaviour very close to the critical point is affected by disorders (Methods).

We show the field-temperature phase diagram for $\left|\log\frac{R_\square}{R_c}\right|$ in Fig. 3c. It reveals the 'fan-shape' structure that is widely observed for quantum criticality[29–31]. The Widom line is close to the vertical blue line stemmed from the critical field (Methods). The T^* line and its mirror image (corresponds to $\left|\log\frac{R_\square}{R_c}\right| \approx 0.45$) set the scale for the finite temperature crossover near the MIT, that is, the boundary of the quantum critical region[27]. We have $\frac{dR_\square}{dT} < 0$ inside this region that is correlated with the Pomeranchuk effect discussed below.

Magnetic properties near the MIT

Since the ground and low-energy excited states of the Mott insulator are determined by magnetic interactions, we examine the magnetic properties near the critical point. A magnetic field parallel to the 2D plane couples weakly to spins because of the strong Ising spin–orbit interaction in TMDs[34] (Extended Data Fig. 5). We characterize the magnetization of holes in TMD moiré heterostructures under an out-of-plane magnetic field B by magnetic circular dichroism (MCD)[11] (Methods and Supplementary Information). Figure 4a illustrates the magnetic-field dependence of MCD for several electric fields at 1.6 K. The MCD increases linearly with B at small fields and saturates above B^* (symbols). The saturation field B^* increases with electric field on the metallic side, but is weakly electric-field-dependent (~4–5 T) on the insulating side. The MCD saturation on the two sides arises from different mechanisms. On the metallic side, B^* agrees well with the saturation field of magnetoresistance (Fig. 4c), at which the transport crosses over from metallic to insulating (inset). On the insulating side, B^* reflects the magnetic interaction energy scale. The MCD can be converted to magnetization since at saturation its value corresponds to magnetization of fully polarized spins.

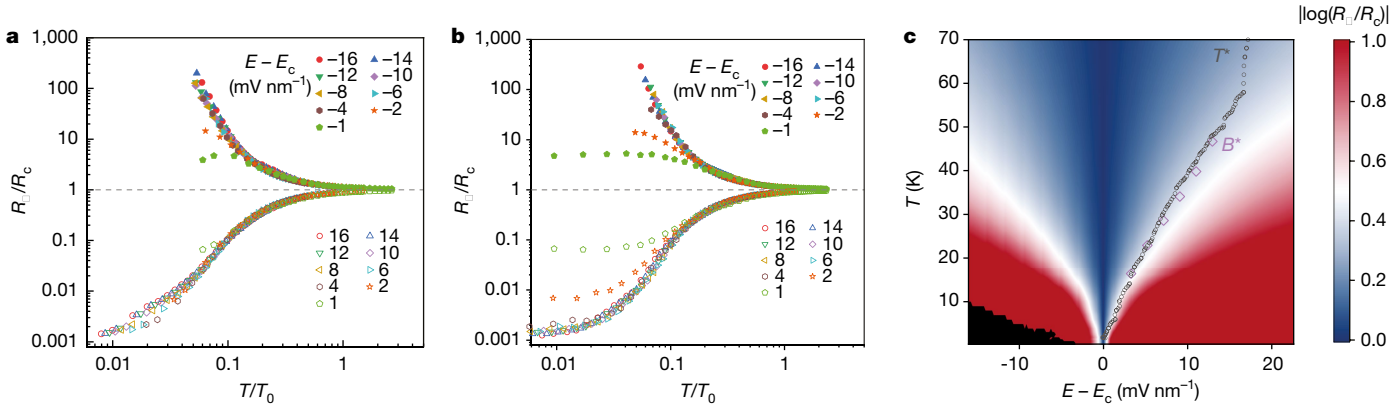

Fig. 3 | Quantum critical scaling. a, **b**, Temperature-dependent square resistance curves near the MIT collapse onto two branches. The resistance curves are scaled by that at the critical field $R_c(T)$; the temperatures are scaled by field-dependent T_0s, as described in the text. Data are obtained from two different rounds of measurements, with one down to 1.6 K (**a**) and the other down to 300 mK (**b**) after different thermal cycles. **c**, Electric field–temperature phase diagram for $\left|\log\frac{R_\square}{R_c}\right|$. The black data points correspond to the crossover temperature T^* from metallic to insulating-like transport. The T^* line and its mirror image (corresponds to $\left|\log\frac{R_\square}{R_c}\right| \approx 0.45$) set the scale for the boundary of the quantum critical region. Purple symbols are the equivalent temperature for the Zeeman energy at the saturation field of the magnetoresistance.

Next we obtain the magnetic susceptibility χ from the slope of the magnetization around $B = 0$. Figure 4b shows the temperature dependence of χ^{-1} at varying electric fields. It is smooth for all electric fields down to 1.6 K. At high temperatures, the data is well described by the Curie–Weiss dependence $\chi^{-1} \propto T - \theta$(dashed lines) with a negative Weiss constant $\theta \approx 30$–40 K for all fields (Supplementary Information). This reflects an antiferromagnetic superexchange interaction between the local moments in the Hubbard model[2] and reveals a magnetic interaction energy of ~3 meV on both sides near the MIT (consistent with the measured B^* on the insulating side in Fig. 4a). Figure 4b also shows substantial magnetic susceptibility at low temperatures on both sides near the MIT. On the metallic side, the onset of susceptibility saturation occurs around

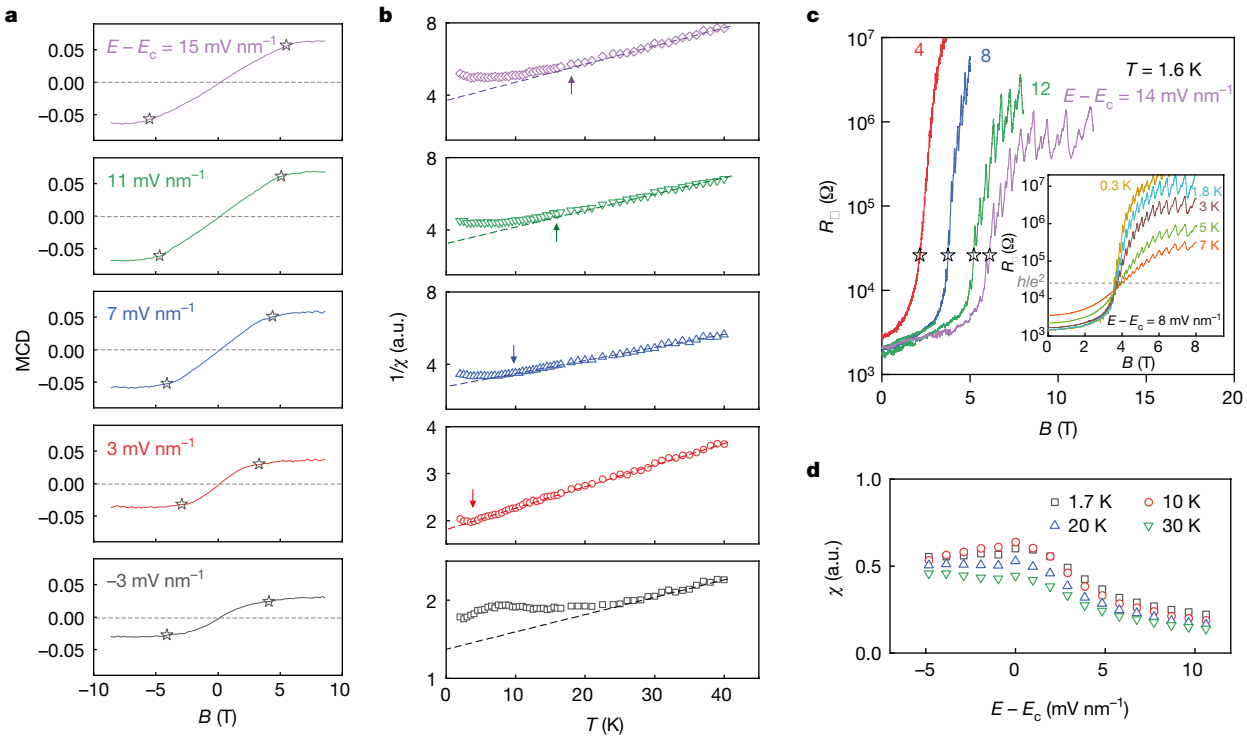

Fig. 4 | Magnetic properties near the Mott transition. a, MCD as a function of out-of-plane magnetic field B under varying electric fields at 1.6 K. It increases linearly with B for small fields and saturates at B^* (symbols). **b**, Temperature dependences of inverse magnetic susceptibility χ^{-1} at varying electric fields. They follow the Curie–Weiss dependences (dashed lines) at high temperatures and saturate at low temperatures for all fields on both sides of the MIT. On the metallic side, the crossover temperatures (denoted by arrows) are associated with the evolution from a Fermi liquid to an incoherent metal. **c**, Magnetoresistance at varying electric fields above the critical electric field (1.6 K). Inset: magnetoresistance at varying temperatures for one of the electric fields; a magnetic-field-induced MIT is observed. The crossover magnetic-field value is used to estimate the saturation field B^* (symbols) in the main panel. It agrees well with the value from the MCD measurement in **a**. The quantum oscillations observed in magnetoresistance are associated with quantum oscillations in the top graphite gate (see Methods for details). **d**, Smooth evolution of magnetic susceptibility at varying temperatures across the MIT, supporting the absence of magnetic phase transition.

T^* (marked by arrows). The magnetic susceptibility also shows a smooth dependence on electric field across the MIT down to 1.6 K (Fig. 4d).

At low temperatures, the system is a Landau Fermi liquid on the metallic side; χ is given by the Pauli susceptibility of the heavy fermions near the Fermi surface[3]. Above ~T^*, the system enters an incoherent regime; local moments emerge; the susceptibility follows the Curie–Weiss dependence. This is correlated with the crossover from metallic ($\frac{dR_\square}{dT} > 0$) to insulating-like ($\frac{dR_\square}{dT} < 0$) transport upon heating across T^* (Fig. 2a and Extended Data Fig. 6). The behaviour is reminiscent of the Pomeranchuk effect observed in helium-3, in which the increasing localization of charges and formation of local moments lead to an increase in spin entropy upon heating[23,31,35]. The coherent quasiparticles can also be destroyed when the Zeeman energy overcomes the renormalized bandwidth[3] ($g\mu_B B^* \gtrsim W^*$; Methods). This picture is consistent with the magnetoresistance data in Fig. 4c and is further supported by the good agreement between $g\mu_B B^*$ and the thermal excitation energy ($k_B T^* \approx W^*$) in Fig. 3c. Here g, μ_B and k_B denote the hole g factor ($g \approx 11$ in TMDs[36]), the Bohr magneton, and the Boltzmann constant, respectively. Compared to most 2D electron systems[28,37], the hole Zeeman energy in TMD moiré superlattices is substantially larger than the cyclotron energy[38] because of the large g factor and the heavy band mass that is further enhanced by the moiré flat bands.

Near the MIT, the magnetic interaction energy (~3 meV) sets the smallest energy scale of the system since both U and W are tens of meV. The lowest measurement temperature (1.6 K and 300 mK for magnetic and transport properties, respectively) is well below this energy scale. Therefore, the smooth temperature dependence of χ without any sign of spin gap for all electric fields (Fig. 4b) and the smooth evolution of χ across the MIT (Fig. 4d) support the absence of long-range magnetic order on both sides. These observations point to a MIT from a Fermi liquid to a nonmagnetic (or 120-degree Néel below 1.6 K) Mott insulator with extensive spin entropy at finite temperatures. This is expected for a frustrated lattice[4,23,30,31] and further corroborated by the Pomeranchuk effect. Moreover, since m^* diverges on the metallic side, the smooth evolution of χ across the MIT implies a diverging Landau-parameter, F_0^a, and similarly, a diverging F_0^s as the compressibility must vanish at the MIT[4].

Conclusions

In conclusion, we have demonstrated a continuous Mott transition in $MoTe_2/WSe_2$ moiré superlattices down to 300 mK and performed scaling analyses near the quantum critical point. The MIT is induced by varying an out-of-plane electric field that modifies predominantly the moiré potential depth and thus U/W. Our results, including a continuously vanishing charge gap, diverging effective mass, constant spin susceptibility across the MIT, and the Pomeranchuk effect, point to a clear example of a continuous MIT across which the entire electronic Fermi surface disappears abruptly. In addition, because the half-band filling density is nearly two orders of magnitude higher than the disorder density, disorder only plays a perturbative role in the observed interaction-driven MIT. Remarkable similarity to the density-tuned MITs in 2D electron gas systems that have very different energy scales and do not have a lattice[3,28,37] has been observed, highlighting the universality of the transition. Future investigations of the transport and magnetic properties near the transitions, particularly at lower temperatures, may reveal new exotic states of matter such as quantum spin liquids.

Online content

Any methods, additional references, Nature Research reporting summaries, source data, extended data, supplementary information, acknowledgements, peer review information; details of author contributions and competing interests; and statements of data and code availability are available at https://doi.org/10.1038/s41586-021-03853-0.

1. Imada, M., Fujimori, A. & Tokura, Y. Metal-insulator transitions. *Rev. Mod. Phys.* **70**, 1039–1263 (1998).
2. Georges, A., Kotliar, G., Krauth, W. & Rozenberg, A. J. Dynamical mean-field theory of strongly correlated fermion system and the limit of infinite dimensions. *Rev. Mod. Phys.* **68**, 13–125 (1996).
3. Dobrosavljević, V., Trivedi, N. & Valles, J. M. Jr *Conductor-Insulator Quantum Phase Transitions* (Oxford Univ. Press, 2012).
4. Senthil, T. Theory of a continuous Mott transition in two dimensions. *Phys. Rev. B* **78**, 045109 (2008).
5. Balents, L. Spin liquids in frustrated magnets. *Nature* **464**, 199–208 (2010).
6. Mishmash, R. V., González, I., Melko, R. G., Motrunich, O. I. & Fisher, M. P. A. Continuous Mott transition between a metal and a quantum spin liquid. *Phys. Rev. B* **91**, 235140 (2015).
7. Szasz, A., Motruk, J., Zaletel, M. P. & Moore, J. E. Chiral spin liquid phase of the triangular lattice hubbard model: a density matrix renormalization group study. *Phys. Rev. X* **10**, 021042 (2020).
8. Qi, Y. & Sachdev, S. Insulator-metal transition on the triangular lattice. *Phys. Rev. B* **77**, 165112 (2008).
9. Wu, F., Lovorn, T. Tutuc, E. & MacDonald, A. H. Hubbard Model physics in transition metal dichalcogenide moiré bands. *Phys. Rev. Lett.* **121**, 026402 (2018).
10. Regan, E. C. et al. Mott and generalized Wigner crystal states in WSe_2/WS_2 moiré superlattices. *Nature* **579**, 359–363 (2020).
11. Tang, Y. et al. Simulation of Hubbard model physics in WSe_2/WS_2 moiré superlattices. *Nature* **579**, 353–358 (2020).
12. Shimazaki, Y. et al. Strong correlated electrons and hybrid excitons in a moiré heterostructure. *Nature* **580**, 472–477 (2020).
13. Wang, L. et al. Correlated electronic phases in twisted bilayer transition metal dichalcogenides. *Nat. Mater.* **19**, 861–866 (2020).
14. Xu, Y. et al. Correlated insulating states at fractional fillings of moiré superlattices. *Nature* **587**, 214–218 (2020).
15. Jin, C. et al. Stripe phases in WSe_2/WS_2 moiré superlattices. *Nat. Mater.* **20**, 940–944 (2021).
16. Huang, X. et al. Correlated insulating states at fractional fillings of the WS_2/WSe_2 moiré lattice. *Nat. Phys.* **17**, 715–719 (2021).
17. Balents, L., Dean, C. R., Efetov, D. K. & Young, A. F. Superconductivity and strong correlations in moiré flat bands. *Nat. Phys.* **16**, 725–733 (2020).
18. Andrei, E. Y. & MacDonald, A. H. Graphene bilayers with a twist. *Nat. Mater.* **19**, 1265–1275 (2020).
19. Zhang, Y., Yuan, N. F. Q. & Fu, L. Moiré quantum chemistry: charge transfer in transition metal dichalcogenide superlattices. *Phys. Rev. B* **102**, 201115(R) (2020).
20. Pan, H., Wu, F. & Das Sarma, S. Quantum phase diagram of a moiré-Hubbard model. *Phys. Rev. B* **102**, 201104(R) (2020).
21. Morales-Durán, N., Potasz, P. & MacDonald, A. H. Metal-insulator transition in transition metal dichalcogenide heterobilayer moiré superlattices. *Phys. Rev. B* **103**, L241110 (2021).
22. Pan, H. & Das Sarma, S. Interaction-driven filling-induced metal-insulator transition in 2D moiré lattices. *Phys. Rev. Lett.* **127**, 096802 (2021).
23. Wietek, A. et al. Mott insulating states with competing orders in the triangular lattice Hubbard model. Preprint at https://arxiv.org/abs/2102.12904 (2021).
24. Brinkman, W. F. & Rice, T. M. Application of Gutzwiller's variational method to the metal-insulator transition. *Phys. Rev. B* **2**, 4302–4304 (1970).
25. Florens, S. & Georges, A. Slave-rotor mean-field theories of strongly correlated systems and the Mott transition in finite dimensions. *Phys. Rev. B* **70**, 035114 (2004).
26. Yang, H. Y., Läuchli, A. M., Mila, F. & Schmidt, K. P. Effective spin model for the spin-liquid phase of the Hubbard model on the triangular lattice. *Phys. Rev. Lett* **105**, 267204 (2010).
27. Terletska, H., Vučičević, J., Tanasković, D. & Dobrosavljević, V. Quantum critical transport near the Mott transition. *Phys. Rev. Lett* **107**, 026401 (2011).
28. Spivak, B., Kravchenko, S. V., Kivelson, S. A. & Gao, X. P. A. *Colloquium*: Transport in strongly correlated two dimensional electron fluids. *Rev. Mod. Phys.* **82**, 1743–1766 (2010).
29. Vučičević, J., Terletska, H., Tanasković, D. & Dobrosavljević, V. Finite-temperature crossover and the quantum Widom line near the Mott transition. *Phys. Rev. B* **88**, 075143 (2013).
30. Furukawa, T., Miyagawa, K., Taniguchi, H., Kato, R. & Kanoda, K. Quantum criticality of Mott transition in organic materials. *Nat. Phys.* **11**, 221–242 (2015).
31. Pustogow, A. et al. Quantum spin liquids unveil the genuine Mott state. *Nat. Mater.* **17**, 773–777 (2018).
32. Kadowaki, K. & Woods, S. B. Universal relationship of the resistivity and specific heat in heavy-Fermion compounds. *Solid State Comm.* **58**, 507–509 (1986).
33. Emery, V. J. & Kivelson, S. A. Superconductivity in bad metals. *Phys. Rev. Lett.* **74**, 3253–3256 (1995).
34. Xiao, D., Liu, G. B., Feng, W., Xu, X. & Yao, W. Coupled spin and valley physics in monolayers of MoS_2 and other group-VI dichalcogenides. *Phys. Rev. Lett.* **108**, 196802 (2012).
35. Werner, F., Parcollet, O., Georges, A. & Hassan S. R. Interaction-induced adiabatic cooling and antiferromagnetism of cold fermions in optical lattices. *Phys. Rev. Lett.* **95**, 056401 (2005).
36. MacNeill, D. et al. Breaking of valley degeneracy by magnetic field in monolayer $MoSe_2$. *Phys. Rev. Lett.* **114**, 037401 (2015).
37. Abrahams, E., Kravchenko, S. V. & Sarachik, M. P. Metallic behavior and related phenomena in two dimensions. *Rev. Mod. Phys.* **73**, 251–266 (2001).
38. Wang, Z., Shan, J. & Mak, K. F. Valley- and spin-polarized Landau levels in monolayer WSe_2. *Nat. Nanotechnol.* **12**, 144–149 (2017).

Methods

Device fabrication

We fabricated angle-aligned $MoTe_2/WSe_2$ devices using the layer-by-layer dry transfer method[39]. The constituent atomically thin flakes were exfoliated from bulk crystals onto Si substrates with a 285 nm oxide layer and picked up by a polycarbonate (PC) stamp in desired sequence. We first released a stack of graphite/hBN layers onto a Si/SiO_2 substrate as the bottom gate. Platinum (Pt) contacts were patterned into Hall bar geometry on hBN by electron-beam lithography and metallization. The second stack consisting of a $MoTe_2/WSe_2$ bilayer and an hBN/graphite top gate was released onto the pre-patterned Pt electrodes. Figure 1a, b shows a schematic side view and an optical micrograph of a typical device. We used angle-resolved optical second-harmonic generation (SHG) spectroscopy[11] to determine the crystal orientations of WSe_2 and $MoTe_2$ monolayers and the twist angle between them in the heterobilayer (Supplementary Information). The devices investigated in this study are zero-degree aligned within ±0.5°. The uncertainty is mainly limited by that of the SHG measurements. We used relatively thin hBN layers (~5 nm) in the top gate. We found that in general thinner hBN layers can sustain a larger breakdown electric field. Screening effects on the MIT from the top graphite gate are negligible.

Several steps were taken to produce high-quality $MoTe_2/WSe_2$ devices. First we kept the Pt contacts thin (~5 nm) to reduce strain on the device. Second, we removed the polymer residues on the bottom gate from Pt electrode fabrication using an atomic force microscope (AFM) in contact mode. Finally, we handled atomically thin $MoTe_2$ flakes inside a nitrogen-filled glovebox with oxygen and water levels below one part per million (ppm) to minimize degradation of $MoTe_2$. The device spatial inhomogeneity was evaluated by probing the transport properties using various source–drain pairs of a multi-terminal device (Extended Data Fig. 7). We have studied a total of four devices. All of them show interaction-tuned MIT at $f = 1$ and 2 but they have varying degrees of sample inhomogeneity. More homogeneous devices allow scaling analysis closer to the quantum critical point. The results for device 1, which has the highest sample homogeneity, are presented in the main text. The results of device 2 are shown in Extended Data Fig. 8.

Electrical measurements

Electrical transport measurements were performed in a closed-cycle ^{4}He cryostat (Oxford TeslatronPT) equipped with a superconducting magnet and a ^{3}He insert (base temperature ~300 mK). Standard low-frequency (<23 Hz) lock-in techniques were used to measure the sample resistance under a small bias voltage of 1–2 mV to avoid sample heating (Supplementary Information). Both the voltage drop at the probe electrode pairs and the source–drain current were recorded (Supplementary Information). Voltage pre-amplifiers with large input impedance (100 MΩ) were used to measure sample resistance up to ~10 MΩ. In addition to transport measurements, we also performed capacitance measurements to characterize the electronic compressibility near the MIT (Supplementary Information).

MCD measurements

Magnetic circular dichroism (MCD) was performed in an Attocube closed-cycle optical cryostat (attoDry2100) down to 1.6 K and under an out-of-plane magnetic field up to 9 T. The optical beam was focused onto the sample using an optical microscope objective (0.8 numerical aperture); the beam diameter was ~1 μm on the device. The reflected light was collected by the same objective and directed to detectors.

We first characterized the MCD spectrum using a broadband tungsten halogen lamp. A combination of a linear polarizer and an achromatic quarter-wave plate was used to generate circularly polarized light. The incident power on the device was kept below 1 nW. The left- or right-handed light reflected from the sample was spectrally resolved by a spectrometer coupled to a liquid-nitrogen-cooled charge coupled device (CCD). The MCD at a given photon energy is defined as $\mathrm{MCD} \equiv (I_L - I_R)/(I_L + I_R)$, where I_L and I_R are the intensity of the left and right circularly polarized light, respectively. A sample MCD spectrum as a function of out-of-plane electric field is shown in Extended Data Fig. 9. The MCD is strongly enhanced near the fundamental exciton resonance of WSe_2; the electric field has a negligible effect on the resonance energy for electric fields near E_c. This allows us to probe the MCD response at a fixed wavelength 747.4 nm (Fig. 4). The optical excitation was provided by a tunable, continuous-wave Ti-sapphire laser (M Squared SOLSTIS system). We limited the incident light power to about 300 nW on the sample to minimize the heating effects. We modulated the light helicity by a photoelastic modulator at 50.1 kHz and detected the reflected light by a photodiode. The MCD signal is defined as the ratio of the modulated signal (measured by a lock-in amplifier) to the total reflected light power (measured by a d.c. voltmeter). To obtain the magnetic susceptibility data in Fig. 4b, d, we further normalized the saturated MCD response at all electric fields to the same value. This is justified because the saturated magnetization at $f = 1$ is expected to be independent of electric field. Additional control experiments and spectrum analysis are described in the Supplementary Information.

Band structure calculations

Density functional calculations were performed using Perdew–Burke–Ernzerhof generalized gradient approximation[40] with the van der Waals correction incorporated by DFT-D3 method with Becke–Jonson damping[41] as implemented in the Vienna Ab initio Simulation Package[42]. Pseudopotentials were used to describe the electron–ion interactions. We first constructed the zero-degree-aligned $MoTe_2/WSe_2$ heterobilayer with vacuum spacing larger than 20 Å to avoid artificial interaction between the periodic images along the out-of-plane direction. The structure relaxation was performed with force on each atom less than 0.01 eV Å^{-1}. We used Gamma-point sampling for structure relaxation and self-consistent calculation. Two representative band structures are shown in Fig. 1d. Additional band structures at different displacement fields are included in the Supplementary Information.

We limited the band structures to five k points along the Γ–M direction and 15 k points connecting K–Γ–M–K. This is sufficient to determine the moiré bandgap and bandwidth since they are given by energies at the high-symmetry points. The moiré band structure is developed from the Γ valley of monolayer $MoTe_2$ and WSe_2 (note that the energy ordering of Γ and K valleys is sensitive to the specific van der Waals functional; effects from different functionals require further in-depth studies). The moiré band maximum and minimum are expected to be at the Γ and K points of the mini-Brillouin zone, respectively, similar to other TMD moiré systems[9]. As a result, the first moiré bandwidth can be estimated from the energy difference between the Γ point (maximum) and the K point (minimum). The moiré bandgap can be estimated in a similar manner. When the moiré bandgap closes, there remains only a single touching point for the two moiré bands. The first moiré band remains well defined and the bandwidth can be estimated using the same method.

Figure 1e shows the moiré bandgap and the first moiré bandwidth as a function of out-of-plane displacement field, D. The displacement field is related to the applied electric field, $D = \varepsilon_{\mathrm{TMD}} E$, through the out-of-plane dielectric constant $\varepsilon_{\mathrm{TMD}}$ of the TMD heterobilayer. We estimate $\varepsilon_{\mathrm{TMD}} \approx 7$–$8$ from the measured interlayer dipole moment ~2.6 eÅ by optical spectroscopy (Supplementary Information). Because of interlayer hybridization, $\varepsilon_{\mathrm{TMD}}$ is expected to be electric-field dependent; D and E are not expected to scale linearly over the entire field range.

The closing of the moiré gap and the increase of the bandwidth (near $D \approx 2$ V nm^{-1}) are driven by layer hybridization, which becomes important when the valence band maximum offset between $MoTe_2$ and WSe_2 becomes comparable to the interlayer hopping amplitude (which itself

is dependent on band offset). The energy eigenstates are in general layer-hybridized. Interlayer hybridization, however, does not modify the filling factor of the moiré unit cell or the first moiré band. This gap closing process is also expected to be smooth. The rapid change near $D \approx 2$ V nm^{-1} in Fig. 1e probably reflects the less accurate DFT calculations under high displacement fields. In this regime, the convergence of self-consistent calculations becomes slow, which may result in the rapid change. The DFT calculation is therefore only able to capture the trend of the dependence that is in qualitative agreement with experiment.

Lattice reconstruction and periodic strain in monolayers have been shown to dominate the moiré potential in TMD moiré systems of relatively large moiré period[43,44]. Our results indicate that interlayer hopping (hybridization) is also important in modifying the moiré band structure or the moiré potential strength in angle-aligned $MoTe_2$/WSe_2 heterostructures of relatively small moiré period (~5 nm). The z-direction corrugation is about 0.5 Å after lattice relaxation. In the absence of an out-of-plane electric field, the interlayer hybridization is negligible because of the large band offset. The moiré potential is mostly determined by lattice reconstruction and periodic strain in the monolayers. Under a large field, the contribution to the moiré potential from interlayer hopping increases (which alone would give rise to a larger moiré potential amplitude). Our experimental results suggest that the two contributions compensate each other (or destructively interfere). As a result, the effective moiré potential decreases when the interlayer hopping increases at large electric fields.

Relative band offset in $MoTe_2$/WSe_2 heterobilayers

We determine the relative band offset in $MoTe_2$/WSe_2 heterobilayers by optical measurements (Supplementary Information). The $MoTe_2$ valence band maximum is ~300 meV above the WSe_2 valence band maximum in the absence of electric field; it remains ≥100 meV at the highest electric field applied in this study.

Dependence of U and W on the moiré potential strength V_M

We can estimate how U and W scale with V_M, which is tuned by the electric field. The harmonic-like moiré trapping potential supports an s orbital with a Gaussian wavefunction of size $\xi = \sqrt{a_M}\left(\frac{\pi^4 m V_M}{\hbar^2}\right)^{-1/4} \propto V_M^{-1/4}$.

Here a_M (≈ 5 nm) is the moiré period, m(≈ $0.5m_0$) is the valence band mass of monolayer $MoTe_2$ (m_0 is the free electron mass) and $\hbar$ denotes the reduced Planck's constant. The on-site Coulomb repulsion is given by $U \approx \frac{e^2}{4\pi\varepsilon\xi} \propto V_M^{1/4}$, which increases very slowly with V_M. Here $\varepsilon \approx 4.5\varepsilon_0$ is the effective permittivity of the background (hBN) and ε_0 denotes the vacuum permittivity. On the other hand, we expect the bandwidth W, which is proportional to the inter-moiré-site hopping and the overlap integral of the neighbouring Wannier functions, to scale exponentially with $\xi \propto V_M^{-1/4}$. It has a much stronger dependence on V_M compared to U. Therefore, changing moiré potential depth predominantly changes the bandwidth.

Effects of the second moiré band

The experimental result in Extended Data Fig. 1 shows that the MIT at $f = 2$ occurs at a smaller electric field than the MIT at $f = 1$. It indicates mixing of the moiré bands by U that leads to Hubbard bands of increasing bandwidths with increasing energy (Supplementary Information). This is supported by recent experimental studies on semiconductor moiré materials[14,45]. However, even in the presence of moiré band mixing the physics near $f = 1$ can still be captured by an effective single-band Hubbard model with renormalized parameters in the Hamiltonian[19,46,47]. In particular, the MIT at $f = 1$ remains very close to a Mott transition. This is supported by Extended Data Fig. 1, which shows that the closing of the $f = 2$ gap at ~0.5 V nm^{-1} does not perturb the $f = 1$ insulating state; it does not change the filling factor of the Hubbard band. Otherwise, the MITs at $f = 1$ and $f = 2$ would occur at nearly the same electric field. We summarize the physical picture in Supplementary Fig. 2.

Effects of disorders

Because of sample inhomogeneities, the scaling collapse of resistance curves in Fig. 3 fails for $|E - E_c| < 1$–2 mV nm^{-1}. We can estimate the disorder density in device 1 as ~$2\varepsilon_{hBN}\varepsilon_0\,|E - E_c| \approx 0.5 - 1 \times 10^{11}$ cm^{-2}. Here $\varepsilon_{hBN} \approx 3$ is the out-of-plane dielectric constant of hBN. The disorder density is about two orders of magnitude smaller than the moiré density. The sample disorders may also cause the deviation of the mass divergence from a power-law dependence for $|E - E_C| \lesssim 1$ mV nm^{-1} in Fig. 2d.

Widom line

We adopted the notion of a generalized Widom line[29] to separate regions of metallic and insulating behaviour in the experimental electric field-temperature phase diagram (Fig. 3c). In the scaling analysis of resistance (Extended Data Fig. 4), we find a simple power-law dependence of $R_\square(T)$ at one particular electric field, which are identified as the 'separatrix' $R_c(T)$ and the critical field E_c. The existence of $R_c(T)$ at a constant electric field implies that the Widom line is close to a vertical line stemmed from E_c in the phase diagram. We verified this by finding the inflection points of logarithmic resistance as a function of electric field ($\frac{d^2(\log R_\square)}{dE^2} = 0$) at different temperatures. The $\log R_\square$ inflection point line has been shown to well represent the Widom line. Extended Data Fig. 4 shows that the inflection points are nearly temperature independent, that is, a vertical Widom line from E_c.

Estimate of the renormalized bandwidth of the heavy Fermi liquid near the MIT

Based on the data in Fig. 2d, m^* is enhanced from the single-particle moiré band mass by at least two orders of magnitude near E_c. We therefore expect the renormalized bandwidth W^* of the heavy Fermi liquid to be greatly reduced from the single-particle bandwidth $W \approx U \approx 70$ meV near E_c (estimated from the Coulomb repulsion energy corresponding to the moiré period). Because m^* is only a property of the Fermi surface, we cannot directly relate $1/m^*$ to W^*. Nevertheless, the substantial reduction in the bandwidth near E_c leads to $W^* \approx g\mu_B B^* \approx k_B T^*$ as shown in Fig. 3c.

Quantum oscillations in the magnetoresistance

The magnetoresistance of the $MoTe_2$/WSe_2 device in Fig. 4c shows Shubnikov–de Hass–like oscillations in addition to the metal–insulator transition. These oscillations are associated with formation of Landau levels in the top graphite gate under an out-of-plane magnetic field. They vanish above ~30 K, which is in good agreement with the reported temperature range for Shubnikov–de Hass oscillations in graphite[48]. They also vanish when we replace graphite by 2D metal $TaSe_2$ in the top gate (Extended Data Fig. 10). The coupling between the closely spaced $MoTe_2$/WSe_2 sample and the top graphite gate (~5 nm) is presumably capacitive, that is, through screening[49]. The energy gap for charge excitations in a 2D insulator is sensitive to its dielectric surroundings[50]. When Landau levels are developed in the nearby graphite gate under a magnetic field, the oscillations in graphite's density of states induce oscillatory changes in the effective dielectric function that the 2D insulator experiences, and consequently, oscillations in the charge-gap and the in-gap resistance (through thermal activation) of the sample. The oscillation amplitude is the largest for in-gap electrical transport (Extended Data Fig. 10).

Data availability

The source data that support the findings of this study are available with the paper. Source data are provided with this paper.

39. Wang, L. et al. One-dimensional electrical contact to a two-dimensional material. *Science* **342**, 614–617 (2013).
40. Perdew, J. P., Burke, K. & Ernzerhof, M. Generalized gradient approximation made simple. *Phys. Rev. Lett.* **77**, 3865–3868 (1996).
41. Grimme, S., Antony, J., Ehrlich, S. & Krieg, H. A consistent and accurate ab initio parametrization of density functional dispersion correction (DFT-D) for the 94 elements H-Pu. *J. Chem.* **132**, 154104 (2010).
42. Kresse, G. & Furthmüller, J. Efficiency of ab-initio total energy calculations for metals and semiconductors using a plane-wave basis set. *Comp. Mat. Sci.* **6**, 15–50 (1996).
43. Shabani, S. et al. Deep moiré potentials in twisted transition metal dichalcogenide bilayers. *Nat. Phys.* **17**, 720–725 (2021).
44. Li, H. et al. Imaging moiré flat bands in three-dimensional reconstructed WSe_2/WS_2 superlattices. *Nat. Mater.* **20**, 945–950 (2021).
45. Li, T. et al. Charge-order-enhanced capacitance in semiconductor moiré superlattices. *Nature Nanotechnol*. https://doi.org/10.1038/s41565-021-00955-8 (2021).
46. Zhang, F. C. & Rice, T. M. Effective Hamiltonian for the superconducting Cu oxides. *Phys. Rev. B* **37**, 3759(R) (1988).
47. Lee, P. A., Nagaosa, N. & Wen, X. G. Doping a Mott insulator: physics of high-temperature superconductivity. *Rev. Mod. Phys.* **78**, 17–85 (2006).
48. Yin, J. et al. Dimensional reduction, quantum Hall effect and layer parity in graphite films. *Nat. Phys.* **15**, 437–442 (2019).
49. Skinner, B. & Shklovskii, B. I. Anomalously large capacitance of a plane capacitor with a two-dimensional electron gas. *Phys. Rev. B* **82**, 155111 (2010).
50. Xu, Y. et al. Creation of moiré bands in a monolayer semiconductor by spatially periodic dielectric screening. *Nat. Mater.* **20**, 645–649 (2021).

Acknowledgements We thank V. Dobrosavljevic, E.-A. Kim, A. H. MacDonald, L. Rademaker and S. Todadri for fruitful discussions. Research was primarily supported by the US Department of Energy (DOE), Office of Science, Basic Energy Sciences (BES), under award no. DE-SC0019481 (electrical measurements) and award no. DE-SC0018945 (band structure calculations). The study was partially supported by the National Science Foundation (NSF) under DMR-1807810 (magneto-optical measurements) and the US Army Research Office under grant number W911NF-17-1-0605 (device fabrication). Growth of the hBN crystals was supported by the Elemental Strategy Initiative of MEXT, Japan and CREST (JPMJCR15F3), JST. This work made use of the Cornell Center for Materials Research Shared Facilities, which are supported through the NSF MRSEC program (DMR-1719875) and the Cornell NanoScale Facility, an NNCI member supported by NSF Grant NNCI-1542081. D.C. acknowledges support from faculty startup grants at Cornell University; K.F.M. acknowledges support from the David and Lucille Packard Fellowship.

Author contributions T.L., S.J. and L.L. fabricated the devices, performed the measurements and analysed the data. K.K. and J.Z. provided assistance in the device fabrication. Y.Z. and L.F. performed the DFT calculations and theoretical analysis. D.C. helped with the theoretical analysis. K.W. and T.T. grew the bulk hBN crystals. T.L., S.J., J.S. and K.F.M. designed the scientific objectives and oversaw the project. All authors discussed the results and commented on the manuscript.

Competing interests The authors declare no competing interests.

Additional information

Supplementary information The online version contains supplementary material available at https://doi.org/10.1038/s41586-021-03853-0.

Correspondence and requests for materials should be addressed to J.S. or K.F.M.

Peer review information *Nature* thanks Lede Xian, You Zhou and the other, anonymous, reviewer(s) for their contribution to the peer review of this work. Peer reviewer reports are available.

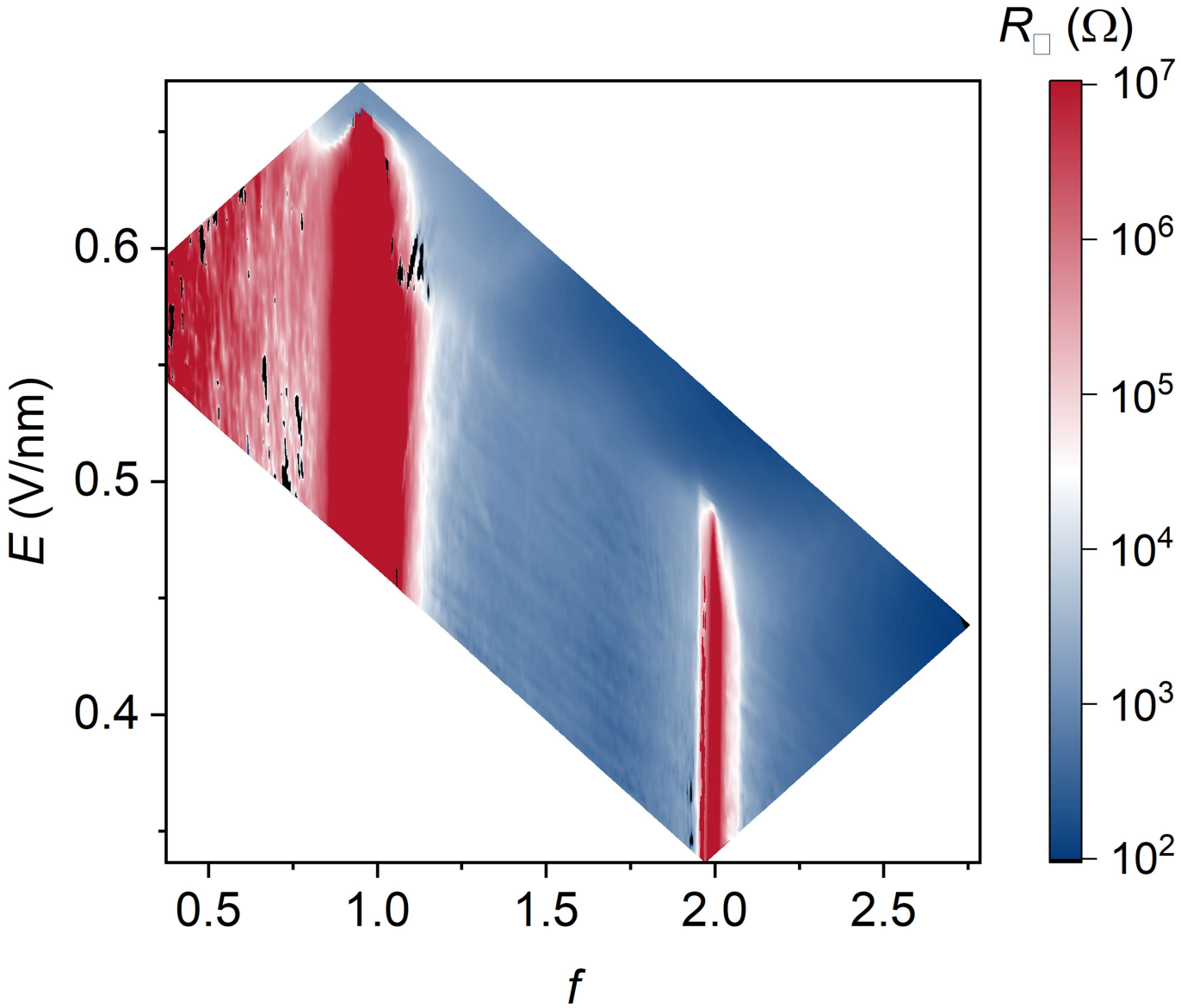

Extended Data Fig. 1 | Square resistance versus electric field and filling factor. 2D map of the square resistance (in log scale) as a function of electric field and filling factor at 300 mK, converted from the data in Fig. 1c. Electric-field-induced MITs are observed at both filling factor $f = 1$ and $f = 2$.

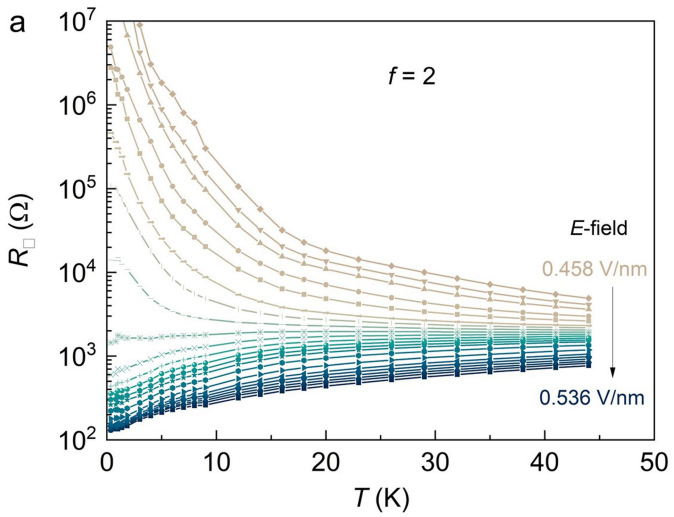

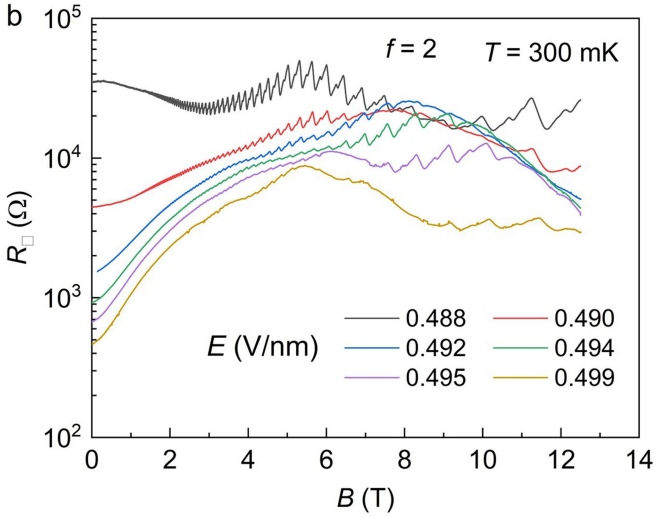

Extended Data Fig. 2 | Metal-insulator transition at $f = 2$. a, Temperature dependence of square resistance at varying electric fields at $f = 2$. MIT is observed near 0.49 V nm^{-1}. Compared to the MIT at $f = 1$, strong effective mass divergence and the Pomeranchuk effect on the metallic side are not observed. **b**, Magnetoresistance at varying electric fields at 300 mK. Compared to the MIT at $f = 1$, magnetic-field-induced metal–insulator transition is not observed.

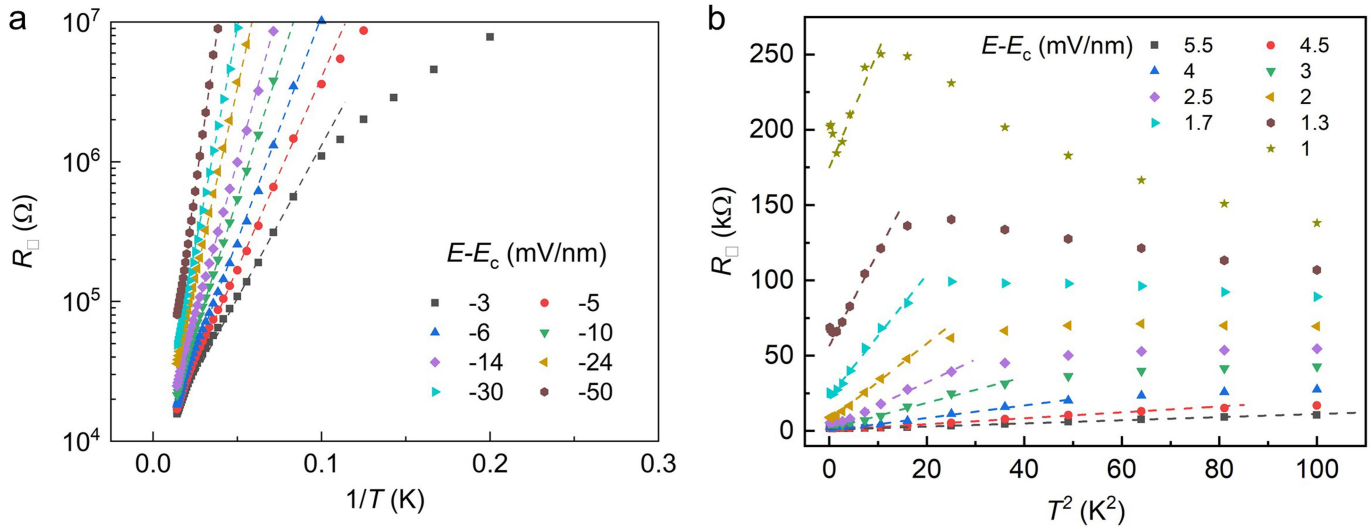

Extended Data Fig. 3 | Extraction of activation gap at $f = 1$ and Landau Fermi liquid behaviour at low temperatures. a, Temperature dependence of the square resistance (symbols) at varying electric fields in an Arrhenius plot. Thermal activation behaviour (dashed lines) is observed at high temperatures, from which the activation gaps are extracted. **b**, Square resistance (symbols) as a function of temperature squared at varying electric fields. The dashed lines are fits at low temperatures to $R_{\square} = R_0 + AT^2$ with fitting parameter R_0 denoting the residual resistance and slope $A \propto (m^*)^2$. The slope increases substantially near the critical electric field. The deviation from the Landau Fermi liquid behaviour at low temperatures very close to the critical point $|E - E_c| < 1$ mV nm^{-1} is likely to be caused by sample disorders. Typical error bars for the applied electric field are ± 0.2 mV nm^{-1}.

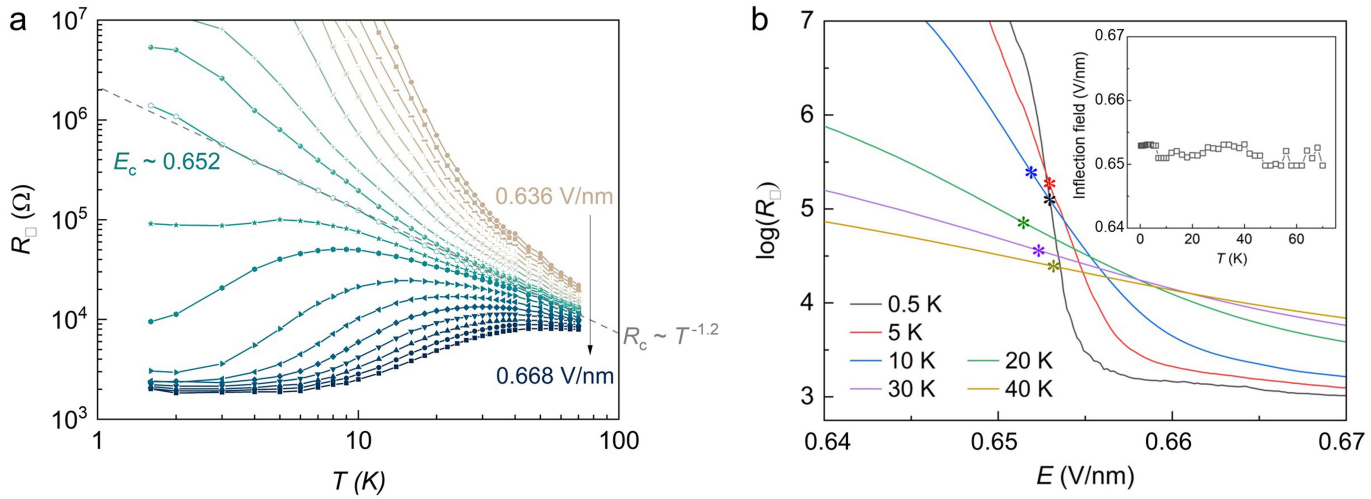

Extended Data Fig. 4 | Resistance scaling at f = 1 near the critical point. **a**, Temperature dependence of square resistance at varying electric fields in a log–log plot. A power-law dependence $\propto T^{-1.2}$ (dashed line) is observed at the critical electric field. **b**, Electric-field dependence of log$R_\square$ at different temperatures. The inflection points are marked by the colour symbols. The inset shows the temperature dependence of the electric field at the inflection point. The data shows that the Widom line is nearly a vertical line in Fig. 3c.

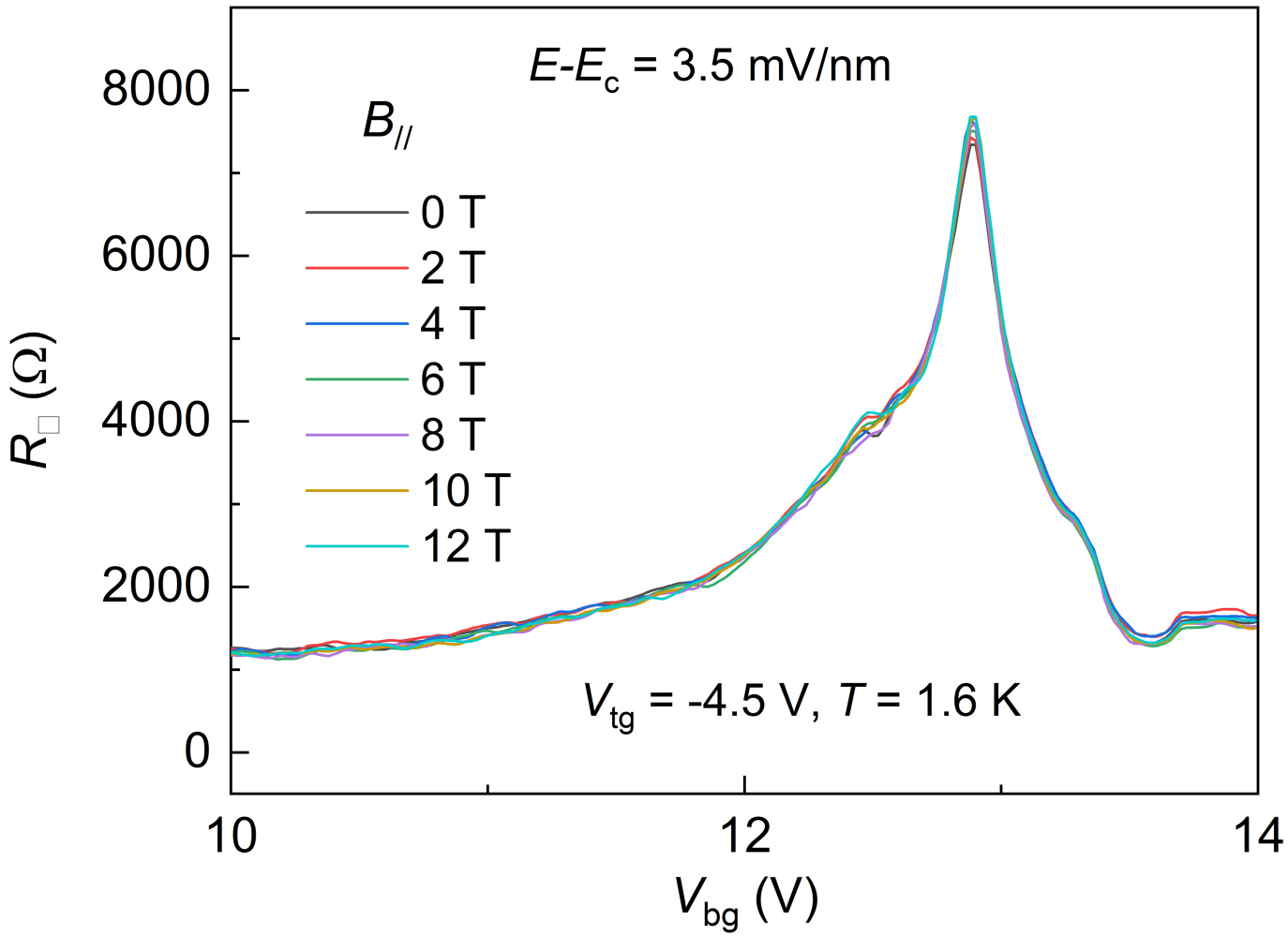

Extended Data Fig. 5 | Absence of in-plane magnetic field dependence. Square resistance as a function of bottom gate voltage at varying in-plane magnetic fields. The bottom gate voltage primarily changes the filling factor f. The electric field is fixed at 3.5 mV nm^{-1} (from E_c) near $f = 1$. No in-plane magnetic field dependence is observed due to the strong Ising spin–orbit coupling in monolayer TMDs.

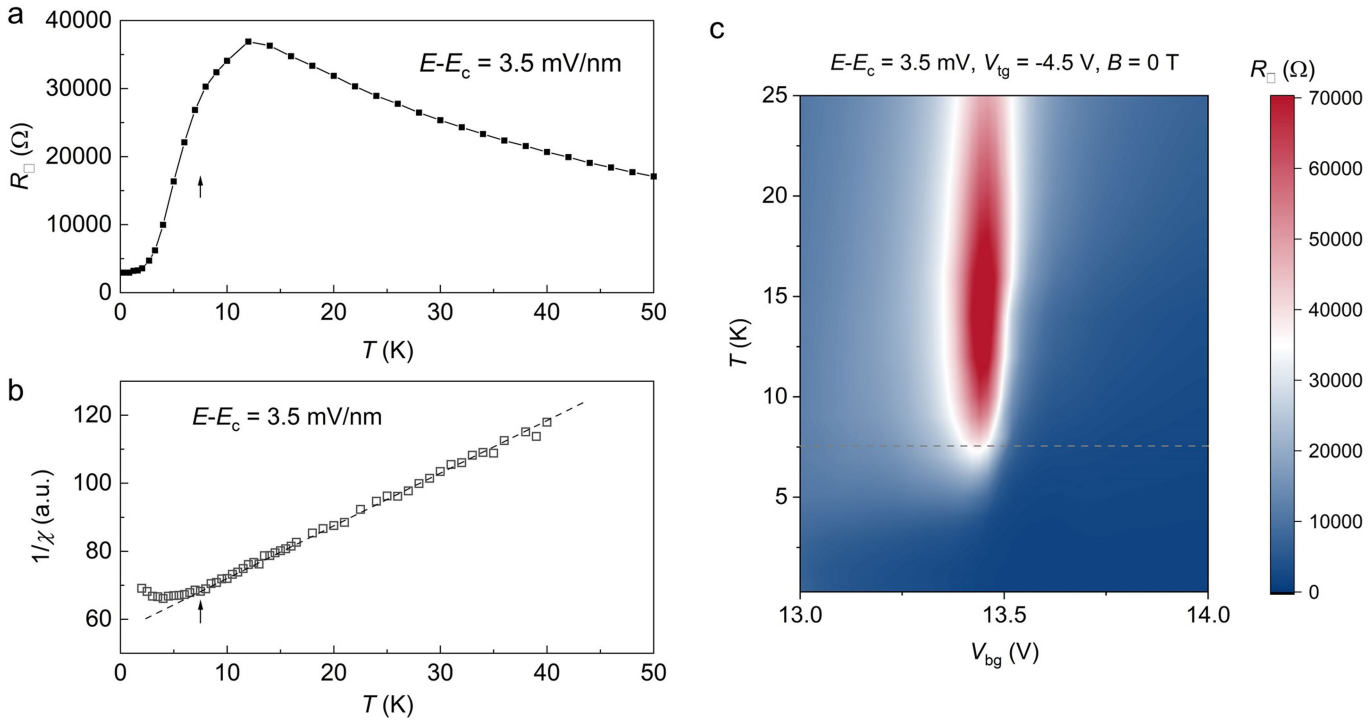

Extended Data Fig. 6 | Pomeranchuk effect at $f=1$. a, Temperature dependence of square resistance at $f=1$ and near 3.5 mV nm^{-1} above the critical field. **b**, Temperature dependence of the inverse magnetic susceptibility under the same condition as **a**. The susceptibility saturates at low temperatures; it follows the Curie–Weiss dependence (dashed lines) above the crossover from a Fermi liquid to an incoherent metal (denoted by the arrow). **c**, Square resistance as a function of temperature and bottom gate voltage at a fixed top gate voltage. The bottom gate voltage mainly changes the filling factor. The electric field is fixed at 3.5 mV nm^{-1} near the $f=1$ resistance peak (with deviations < 0.2 mV nm^{-1}, the typical uncertain in applied electric fields). The $f=1$ resistance peak is absent below ~7 K (horizontal dashed line), where the $R_{\square}-T$ dependence at $f=1$ shows Fermi liquid behaviour (**a**). Above ~7 K but below $T^{*}\approx 16$ K, the $f=1$ resistance peak emerges and the $R_{\square}-T$ dependence deviates from the Fermi liquid behaviour (but still metallic $\frac{dR_{\square}}{dT}>0$). The emergence of the resistance peak and the deviation from the Fermi liquid behaviour are correlated with the emergence of local moments (**b**), demonstrating the Pomeranchuk effect. Above $T^{*}\approx 16$ K, the $f=1$ resistance peak remains but the system displays insulating-like behaviour ($\frac{dR_{\square}}{dT}<0$). The result is fully consistent with the results presented in the main text, where the filling factor is kept constant at $f=1$.

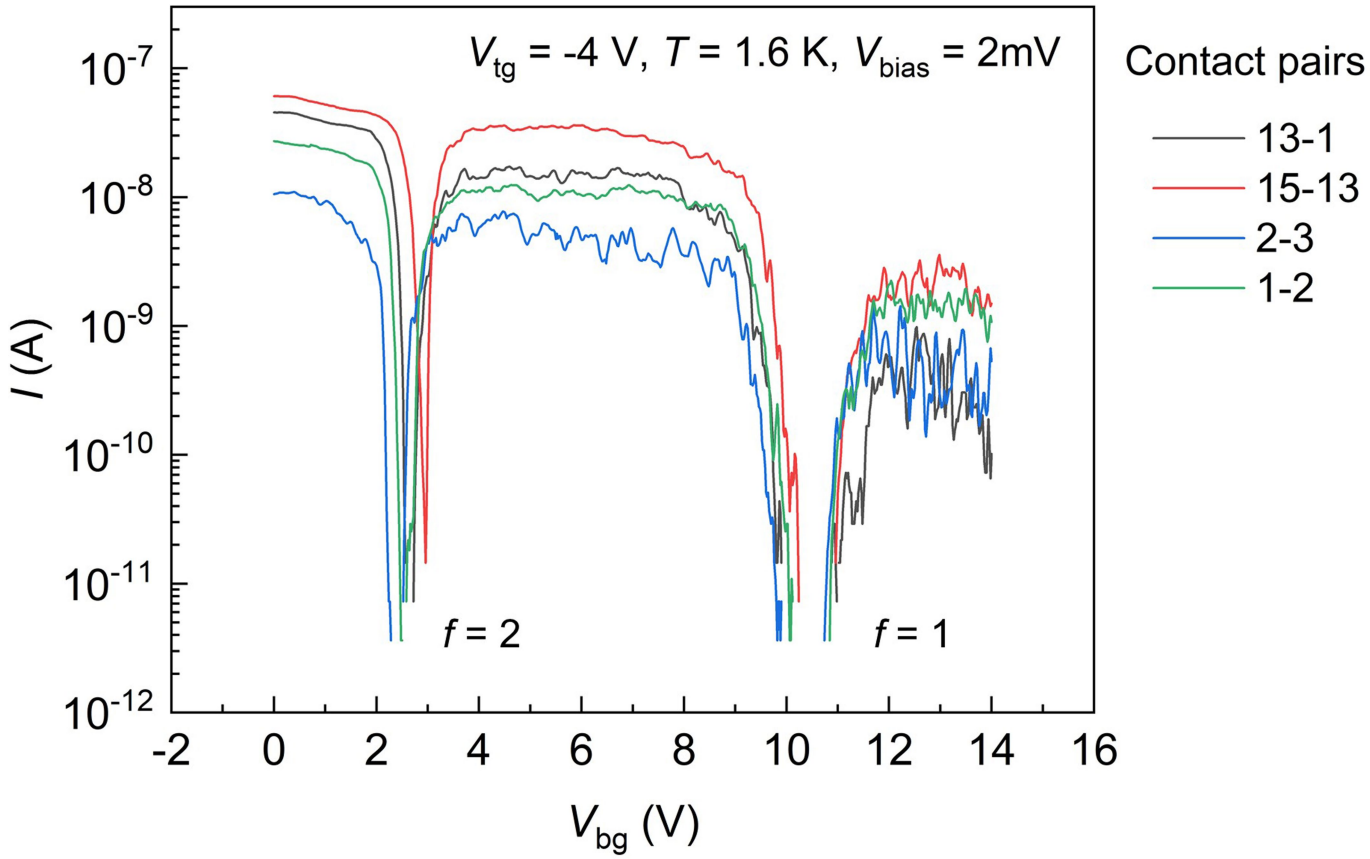

Extended Data Fig. 7 | Spatial homogeneity of device 1. Two-point current as a function of bottom gate voltage at fixed top gate voltage. The excitation bias voltage is 2 mV. The insulating states at $f = 1$ and $f = 2$ are seen at different source–drain pairs corresponding to the optical image in Fig. 1b. The slight shift of the insulating states in gate voltage manifests sample inhomogeneity. The two-point resistance also varies from pair to pair, reflecting the variation in contact/sample resistance.

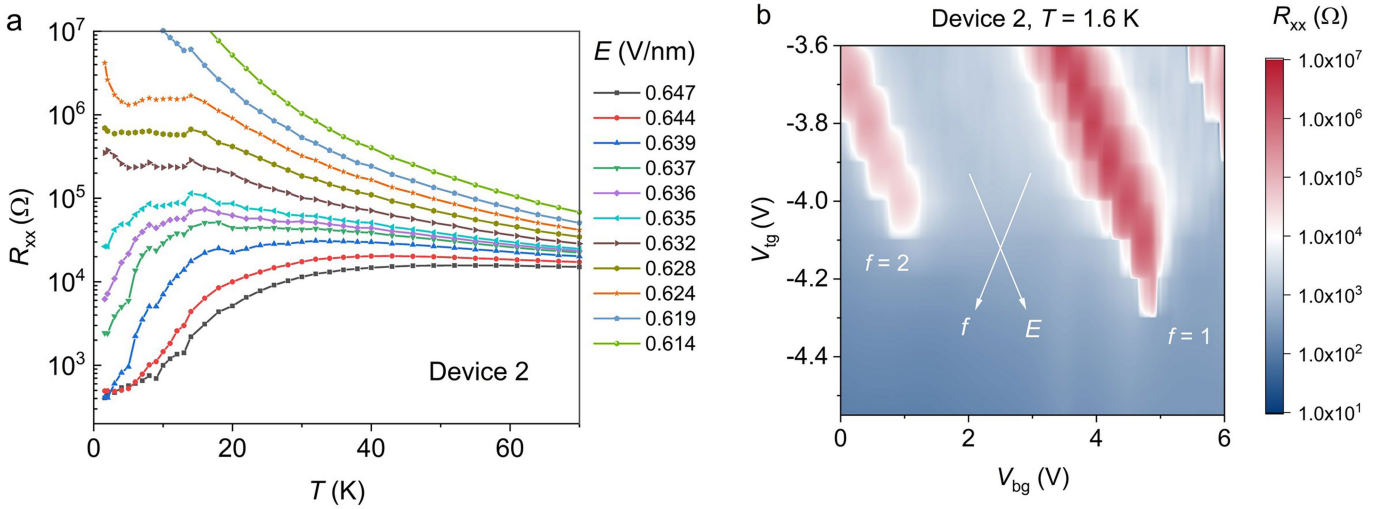

Extended Data Fig. 8 | Major results for device 2. a, Temperature dependence of the longitudinal resistance at $f = 1$ under varying electric fields. The critical electric field is near $E_C = 0.63$ V nm^{-1}. A MIT similar to that in device 1 is observed. **b**, Longitudinal resistance at 1.6 K in logarithmic scale as a function of top and bottom gate voltages. The gate voltages relate to the hole filling factor f and the applied electric field E. Electric-field-induced MIT is observed at $f = 1$ and 2. Compared to device 1, there is a higher degree of spatial inhomogeneity in device 2, which prevents reliable scaling analysis near the critical point.

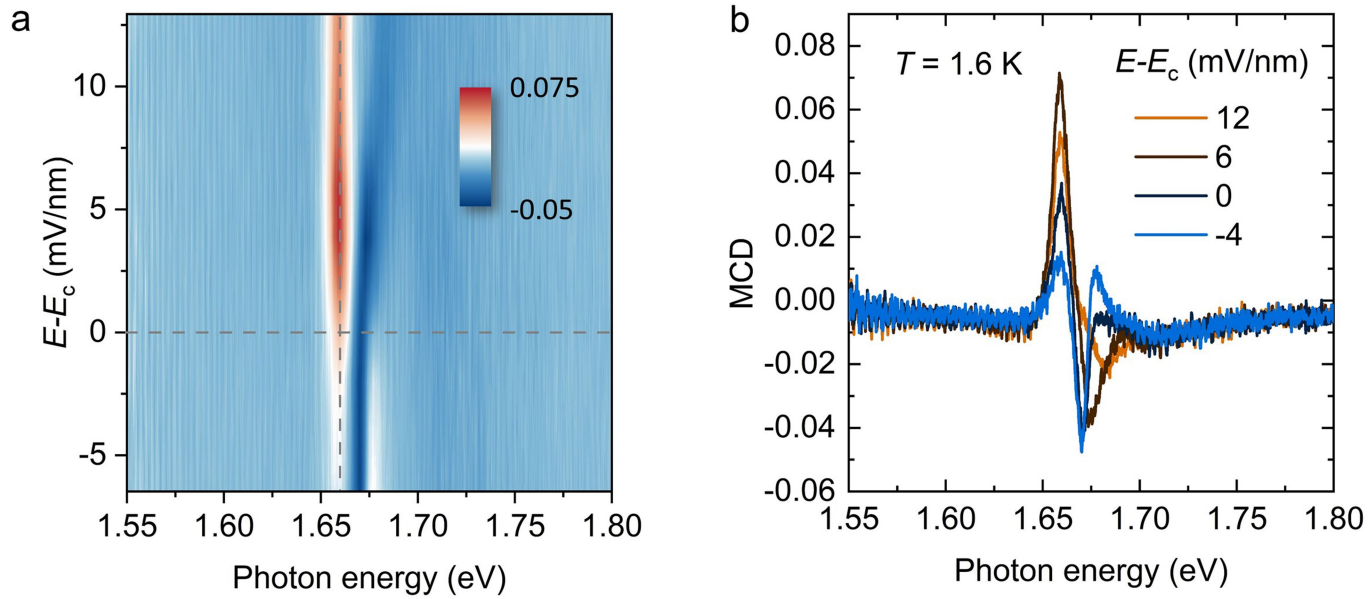

Extended Data Fig. 9 | MCD spectrum under a perpendicular magnetic field of 3 T. a, Electric-field dependence of the MCD spectrum near the WSe_2 exciton resonance. Resonance enhancement is observed near 1.66 eV. The vertical dashed line marks the photon energy of the probe laser beam used for the MCD measurements in Fig. 4 and the horizontal dashed line marks the critical point for the MIT. **b**, MCD spectra at selected electric fields illustrating the resonance enhancement near the exciton peak.

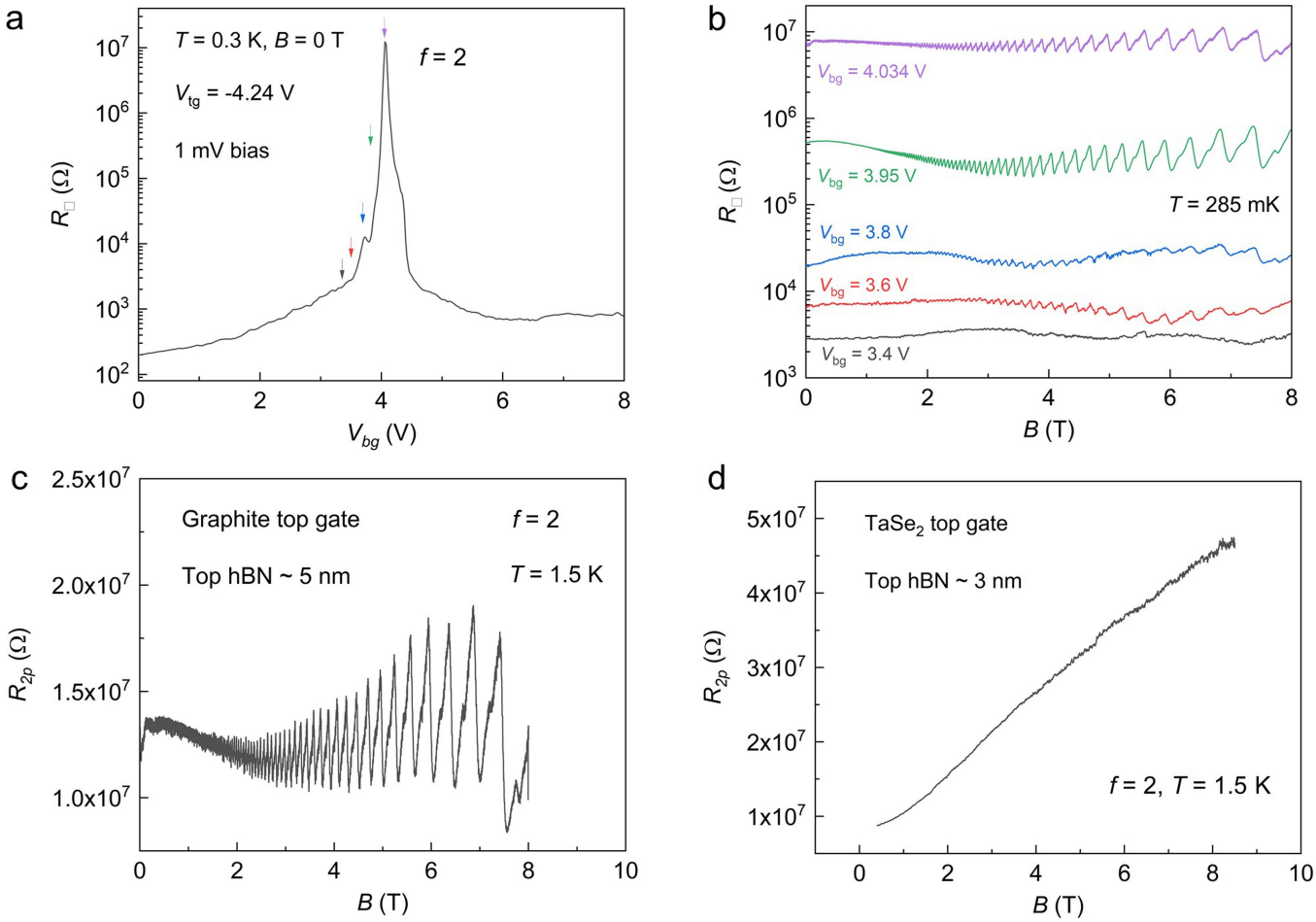

Extended Data Fig. 10 | Quantum oscillations in the insulating states. **a**, Square resistance as a function of bottom gate voltage at 300 mK. The $f = 2$ insulating state is labeled. **b**, Magnetoresistance under a perpendicular magnetic field at selected bottom gate voltages marked by the arrows in **a**. Quantum oscillations due to the nearby graphite gate are observed near the insulating state. The oscillations disappear away from the $f = 2$ insulating state. **c**, Two-terminal magnetoresistance at the $f = 2$ insulating state with a graphite gate about 5 nm separated from the sample. **d**, The same as in **c** except the graphite gate is replaced by a few-layer metallic $TaSe_2$ gate that is ~3 nm away from the sample. No quantum oscillations are developed in both the $TaSe_2$ gate and in the sample under magnetic fields up to 9 T. The results verify that the quantum oscillations are originated from the high mobility graphite gate.